

Article

Experimental Investigation of TR-UHPC Composites and Flexural Behavior of TR-UHPC Composite Slab

Jiuzhi Fu ¹, Yang Zhang ¹ and Yanyue Qin ^{1,2,*}

¹ College of Civil Engineering, Hunan University, Changsha 410082, China; fu1999@hnu.edu.cn (J.F.); zhangbridge@hnu.edu.cn (Y.Z.)

² Department of Civil Engineering, The University of Tokyo, Tokyo 113-8656, Japan

* Correspondence: qin-yanyue@g.ecc.u-tokyo.ac.jp

Abstract: In this investigation, the effects of different fabrics with 0.20% carbon fiber textile (CFT), 0.21% glass fiber textile (GFT), and 0.25% basalt fiber textile (BFT) on the properties of TR-UHPC were investigated by axial tensile tests. A bending test of the BFT-UHPC pavement slab was carried out. In terms of axial tensile performance, the fiber textiles ranked in the following sequence: CFT, BFT, and GFT. Additionally, the corresponding increases in the initial cracking strength and ultimate tensile strength were 18.0% and 21.9% for the CFT, 12.0% and 16.0% for the BFT, and only 9.1% and 8.0% for the GFT, respectively. Increasing the textile reinforcement ratio of the BFT from 0.25% to 0.50% improved the cracking stress and peak stress of the specimen by 12.0% and 15.9%, respectively. Moreover, the ultimate strain of the 0.50%-BFT reinforcing case was 1.4 times that of the 0.25%-BFT reinforcing case and 2.6 times that of the unreinforced specimen in terms of ductility. The results of the stacking test on the BFT reinforced UHPC pedestrian slab indicate that the mid-span deflection of the test slab under normal use load is 0.775 mm, which is only 19.8% of the deflection limit. Additionally, the test slab remained in the elastic stage without any cracking. The BFT effectively enhanced the toughness of the UHPC thin slab after cracking. It is expected to be applied as a novel structure to bridge pedestrian slabs, bridge decks, and other thin UHPC members, thereby improving the durability and mechanical properties of bridge structures.

Keywords: Ultra-High-Performance Concrete; fiber textile; pedestrian walkway slab; tensile performance; flexural behavior



Citation: Fu, J.; Zhang, Y.; Qin, Y. Experimental Investigation of TR-UHPC Composites and Flexural Behavior of TR-UHPC Composite Slab. *Appl. Sci.* **2024**, *14*, 3161. <https://doi.org/10.3390/app14083161>

Academic Editor: José António Correia

Received: 13 March 2024

Revised: 4 April 2024

Accepted: 5 April 2024

Published: 9 April 2024



Copyright: © 2024 by the authors. Licensee MDPI, Basel, Switzerland. This article is an open access article distributed under the terms and conditions of the Creative Commons Attribution (CC BY) license (<https://creativecommons.org/licenses/by/4.0/>).

1. Introduction

China has the largest number and scale of bridges in the world [1]. However, many of these bridges were constructed in the 1980s and 1990s, and as a result, they have been in service for too long to the end of their service life as well as outdated design specifications. Pedestrian walkway slabs, as subsidiary components of bridge decks, are often constructed using reinforced concrete (RC). However, issues such as spalling, the delamination of protective layers, and corrosion of reinforcement commonly occur in RC slabs. These degradation problems are particularly pronounced in marine environments [2,3]. Severe deterioration can significantly impact the overall structural integrity of bridges, while other structures such as galvanized steel pedestrian walkway slabs have a longer lifespan. However, when the steel plates are thin, the structure exhibits low stiffness, resulting in significant deflection and reducing the comfort and safety of pedestrians. On the other hand, increasing the thickness of the steel plates incurs higher economic costs, and the added self-weight significantly reduces the structural safety.

Ultra-high-performance concrete (UHPC), as a new generation of building material emerging in the late 20th century, possesses outstanding properties such as ultra-high strength [4,5] and high toughness [6]. Its exceptional durability is particularly noteworthy, enabling it to effectively adapt to corrosive environments [7]. In recent years, UHPC has

gradually been adopted in China as a primary construction material for main bridge structures [8,9], pedestrian walkway covers [10,11], bridge decks [12,13], and other applications, showcasing broad prospects for its usage. By leveraging existing research, applying UHPC with its high strength, toughness, and durability to pedestrian walkway slabs can address the issues of corrosion and insufficient durability commonly associated with conventional RC slabs. Research indicates that the self-weight of pedestrian walkway slabs accounts for approximately 7% in the long-term loads of railway bridges and about 15% for highway bridges [14]. Using UHPC to make ribbed pedestrian walkway slabs is capable of reducing the thickness and self-weight of slabs [15]. According to JTG D62-2018 [16], the prefabricated concrete pedestrian walkway slab should possess a thickness no less than 60 mm. In this thickness, UHPC ribbed slabs can reduce the self-weight by more than 50%, which can improve the long-term performance of main girders by reducing the long-term stress and thus the creep effect. Simultaneously, the high durability of UHPC can reduce the maintenance cost of the bridge and facilitate transportation, emphasizing an economic advantage.

However, unreinforced UHPC slabs are susceptible to cracking, low-load bearing capacity, and brittle failure when subjected to external loads [17,18]. If two or more layers of rebars are arranged in the slab and subjected to both positive and negative bending moments, the slab thickness must be increased to satisfy the requirement on durability, thus increasing the slab's cost and the self-weight of the whole bridge.

Fiber textiles have the advantages of high strength, light weight, and excellent durability [19,20]. Fiber textile reinforced cementitious materials such as textile reinforced UHPC (TR-UHPC) can improve the ductility and enhance the toughness of UHPC. The multi-layer fiber fabric is arranged in the UHPC matrix, which is conducive to the directional distribution of short fibers, and the two cooperate to exert better mechanical properties. [21]. Contamine et al. [22] investigated the vertical tensile mechanical properties of a layer-casted textile reinforced concrete (TRC) composite. The results indicated that defects during casting have little impact on the tensile mechanical properties of the TRC composite when the textile reinforcement ratio is high. Additionally, the test results showed low dispersion. Gong et al. [23] investigated the tensile properties of strain hardening cement-based materials reinforced by carbon fiber textiles (CFTs) where the results indicated that the composite reinforced with continuous fiber textiles and short fiber hybrids exhibited the best mechanical properties. Dong Z et al. [24] investigated the tensile behaviors of textile reinforced mortar (TRM) with different shapes of carbon multifilament yarns and types of matrices. The results showed that the flatter shape of the yarn could significantly improve the utilization of the textiles in the matrix. Wei M [25] conducted experimental and mechanical studies on the flexural behaviors of FRP fabric reinforced ultra-high-performance concrete (UHPC) panels, where the results showed that such formwork could be potentially used in the accelerated construction of critical infrastructure with enhanced crack resistance and an extended service life.

Currently, research on fiber textile reinforced concrete is well-developed. However, the application of fiber textile reinforced UHPC (TR-UHPC) to engineering structures has received little attention. This study aimed to test the tensile properties of UHPC reinforced with various types of fiber textiles (basalt, carbon, and glass fiber textiles—BFT, CFT, and GFT, respectively) to determine the most cost-effective and reinforcing-efficient case. Subsequently, a novel structural type of basalt fiber textile reinforced UHPC (BFT-UHPC) pedestrian walkway thin slab was proposed in this study. The flexural behavior of the BFT-UHPC slab was explored through the stacking test and bending test. The results of the tests can provide a good basis for the application of fiber textiles in the engineering of BFT-UHPC thin slabs.

2. Axial Tensile Performance of TR-UHPC

2.1. Materials

2.1.1. UHPC Matrix

The UHPC used in the test was provided by Hunan Zhonglu Huacheng Bridge Technology Corporation. The main components of the UHPC included silicate cement, quartz sand, quartz powder, silica fume, fly ash, high-efficiency water reducer, and mixed steel fibers. Table 1 shows the UHPC mix proportion. The volume fraction of steel fibers was 2%, comprising end-hooked steel fibers with a diameter of 0.2 mm and a length of 13 mm. These steel fibers had a tensile strength of 2000 MPa and a modulus of elasticity of 200 GPa.

Table 1. UHPC mix proportion.

Constituent	Cement	Silica Fume	Water Reducer	Fly Ash	Quartz Sand	Quartz Powder	Water	Water-Binder Ratio
Mass ratio	1	0.25	0.2	0.1	1.1	0.25	0.243	0.18

The mechanical properties of the UHPC were tested according to the standard test methods given by ‘Standard Test Methods for Physical and Mechanical Properties of Concrete’ (GB/T 50081-2019) [26] and ‘Reactive Powder Concrete’ (GB/T 31387-2015) [27]. The test for cubic compressive strength involved the use of cubic specimens measuring 100 × 100 × 100 mm for the modulus of elasticity test, prismatic specimens measuring 100 × 100 × 300 mm were used, and for the prismatic compressive strength test, prismatic specimens measuring 100 × 100 × 300 mm were used, with three specimens in each experimental set. The axial tensile strength of the UHPC matrix was obtained by the axial tension test conducted on dog-bone shaped specimens, which is introduced in Section 2.2. Table 2 shows the mechanical properties of the UHPC matrix.

Table 2. Mechanical properties of the UHPC.

Materials	f_{cu} /MPa	f_c /MPa	f_t /MPa	E_c /GPa
UHPC (Steam curing 48 h)	143.4	128.94	7.96	42.50

Note: For the UHPC matrix, f_{cu} is the cube compressive strength, f_c is the prismatic compressive strength, f_t is the initial cracking strength, and E_c is the Young’s modulus.

2.1.2. Fiber Textiles

Three kinds of commonly used FRP materials were selected in this test: carbon fiber textile (CFT), basalt fiber textile (BFT), and glass fiber textile (GFT), as shown in Figure 1. The mechanical properties of these fiber textiles and sectional area of a single fiber bundle are shown in Table 3.

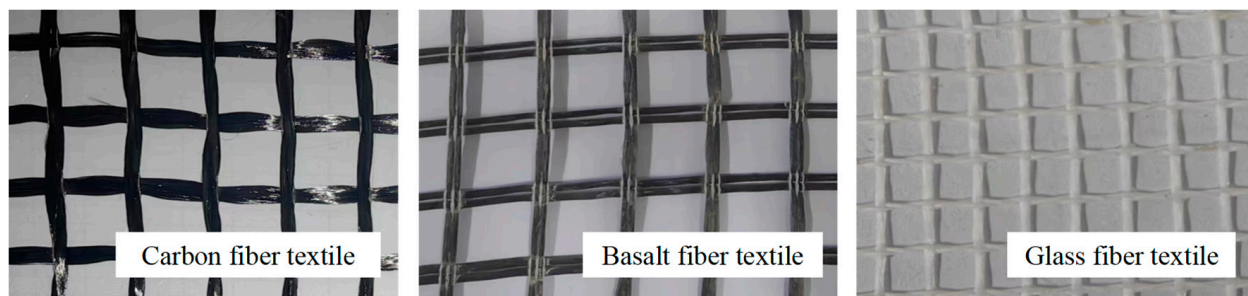


Figure 1. Fiber textiles.

Table 3. Basic mechanical properties of different fiber textiles.

Textile Type	Grid Size (mm × mm)	Young's Modulus (GPa)	Tensile Strength (MPa)	Ultimate Tensile Strain (%)	Single Bundle Sectional Area (mm ²)
CFT	20 × 20	230	3300	2.80	0.88
GFT	3 × 3	71	2204	1.98	0.16
BFT	25 × 25	80	2362	2.77	1.45

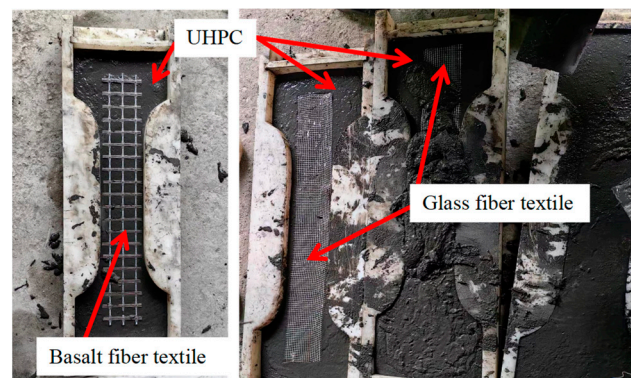
2.2. Specimen Manufacture Process and Experiment Program

Through the axial tension test, the impact of the type and amount of fiber textiles on the tensile properties of the textile-reinforced UHPC (TR-UHPC) was investigated. The tensile specimen was named "T". The capitals "C", "G", and "B" refer to the fiber type, which are the CFT, GFT, and BFT, respectively. The numbers "2" and "4" refer to the number of fiber textile layers. For instance, in "T-B2", "T" refers to tensile test, "B" indicates BFT, and "2" means two layers of textile. The series of tensile specimens are shown in Table 4, with three specimens for each series.

Table 4. Parameters of the TR-UHPC axial tensile test.

Specimen	Fiber Type	Textile Layer Number	Textile Reinforcement Ratio
T-C2	Carbon fiber	2	0.20%
T-G2	Glass fiber	2	0.21%
T-B2/4	Basalt fiber	2/4	0.25%/0.50%
T-U	--	--	--

The casting process is shown in Figure 2. Axial tensile specimens (dog-bone shaped) made of TR-UHPC were manufactured with a tensile section size of 80 × 50 × 150 mm. The spacing between the two-layer and four-layer textile specimens was 10 mm, as shown in Figure 3a. The specimens were cast layer by layer, with the first layer of UHPC cast into the mold up to the marked height. When laying the first layer of the fiber textile, the textile was slightly pressed to make the UHPC surround the textiles. Then, the next layer of UHPC was cast and repeated until the casting was complete. After 48 h from casting, the specimen was demolded and cured in steam at a temperature of 90 °C for 48 h.

**Figure 2.** Manufacturing process of axial tensile specimens.

Carbon fiber reinforced plastic (CFRP) cloths were attached to the sectional area changing part of the dog-bone shaped specimen to make sure the specimen failed at the middle section. A universal testing machine (SHT4605-G, stroke and force limits of 710 mm and 600 kN, respectively) was used to apply tension to the specimen, as shown in Figure 3b.

The two ends of the dog-bone specimen were connected to the testing machine through jigs, and the loading method used was displacement-controlled loading with a loading rate of 0.05 mm/min. The strain before cracking was measured by strain gauges, and the tensile displacement of the specimen after cracking was measured by an electronic extensometer

with a measurement scale of 150 mm. The axial tension test was terminated when the specimen completely fractured.

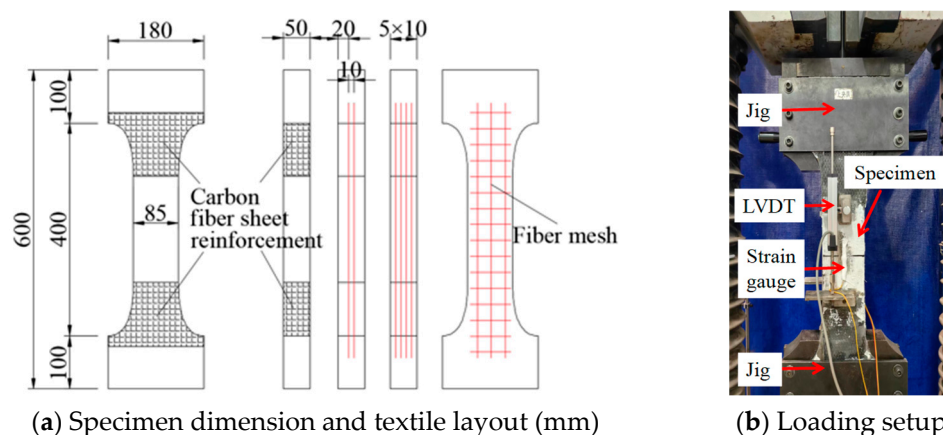


Figure 3. Experiment program and setup of the axial tension test.

2.3. Results and Analyses of Axial Tension Tests

Table 5 shows the results of the TR-UHPC tension tests including the relative standard deviation (RSD) of each series of specimens in brackets. The RSDs of the peak strain were generally higher because the stress fluctuated within a certain range of values after cracking, however, the RSDs of peak strain were still within the acceptable range overall. Regarding RSD, the T-B2 and TB-4 specimens demonstrated a more stable performance compared to the other specimens. The T-C2 specimens had the most fluctuating test results because the textile treatment had a significant impact on the stress distribution within the single bundle and the interface between the fiber bundle and the UHPC matrix [28]. The CFT in the test was not impregnated by the epoxy resin adhesive. As a result, the carbon fiber monofilaments within the single-bundle multifilament yarns could not coordinate well. Additionally, the UHPC matrix could not completely penetrate all of the slots among the monofilaments to establish a good connection with all the monofilaments [29,30]. Consequently, there was no effective bonding between the CFT and UHPC matrix. On the other hand, the untreated CFT has a smooth surface and transfers force to the UHPC mainly through chemical bonding, which will fail once the CFT is stripped.

Table 5. Test results of the axial tension tests.

Specimen Group	Initial Cracking Stress (MPa)	Initial Cracking Strain ($\mu\epsilon$)	Peak Stress (MPa)	Peak Strain ($\mu\epsilon$)
T-U	7.48 (1.4%)	144.5 (7.3%)	7.96 (5.6%)	164.3 (17.7%)
T-G2	8.16 (3.3%)	182.4 (11.0%)	8.60 (3.9%)	222.3 (24.5%)
T-C2	8.83 (12.8%)	213.3 (10.0%)	9.69 (13.2%)	254.3 (20.3%)
T-B2	8.38 (2.5%)	190.5 (2.2%)	9.23 (4.7%)	233.8 (3.4%)
T-B4	8.57 (4.5%)	181.7 (3.2%)	9.80 (2.6%)	8805.5 (15.8%)

2.3.1. Failure Mode

Figure 4 illustrates the failure modes of all tensile specimens. Compared with the plain UHPC axial tensile specimen, the tensile strength of the TR-UHPC composites were substantially increased. As shown in Figure 4, the plain UHPC specimen failed with UHPC matrix fracture and steel fiber pull-out, while the TR-UHPC specimen failed with fiber textile rupture after matrix cracking.

The failure process of the TR-UHPC tensile specimens can mainly divided into three stages: the elastic stage, post-cracking stage, and rupture failure stage. In the elastic stage, the UHPC matrix and the textile are deformed consonantly and subjected to tension. Meanwhile, the modulus of elasticity of the TR-UHPC composite is related to the properties and proportions of the UHPC matrix and the fiber textile. After the UHPC matrix cracked,

the TR-UHPC composites entered the post-cracking stage with an increase in the tension value. Note that only the T-B4 specimens experienced a multi-cracking progress because its textile reinforcement ratio exceeded the critical textile reinforcement ratio reported in reference [31], and the bonding performance between the BFT and UHPC matrix was excellent, which is like suitably reinforced concrete beams. In contrast, the T-B2 specimens with a lower textile reinforcement ratio only had one principal crack during tensioning. T-C2 and T-G2 specimens experienced the same failure mode, that is, fiber textile rupture. Due to the weak bonding performance between the CFT/GFT and UHPC matrix, their crack pattern was single cracking.

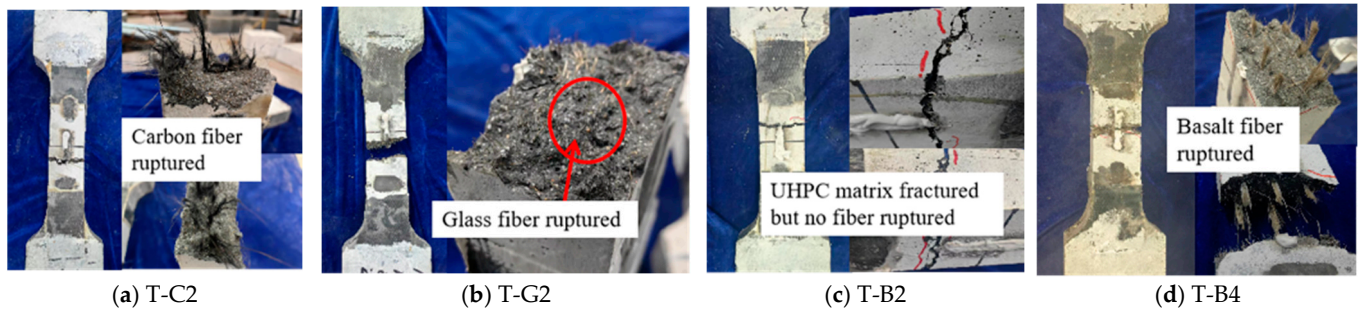


Figure 4. Failure modes of the axial tension tests.

2.3.2. Impact of Fiber Type on Tensile Properties of TR-UHPC Composites

Figure 5 shows a comparison of the stress–strain curves between various TR-UHPC tensile specimens.

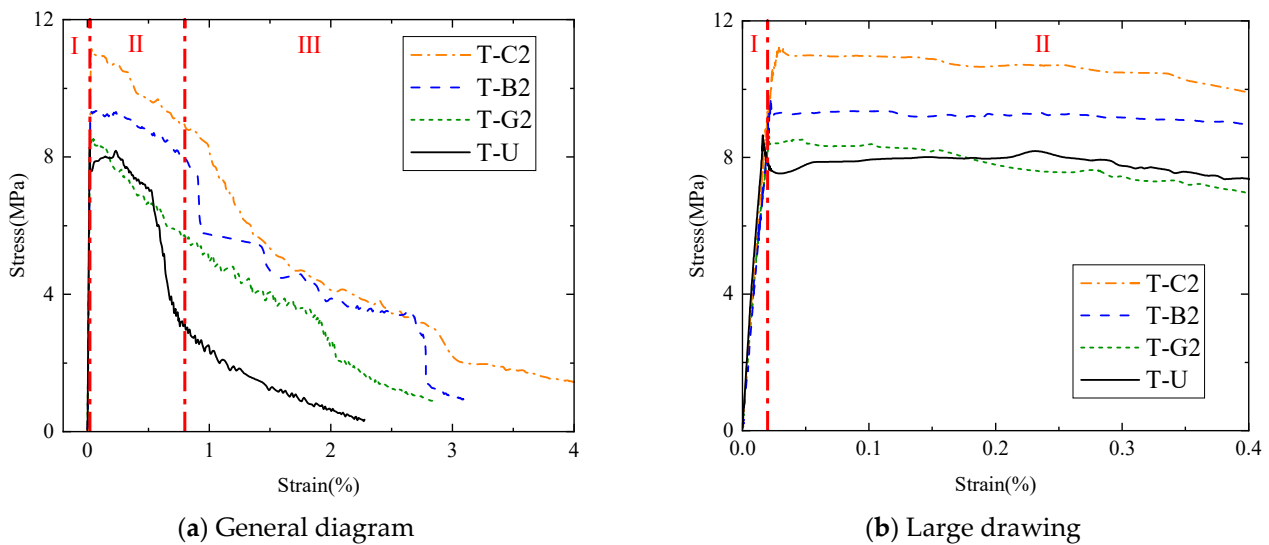


Figure 5. Comparison of the stress–strain curves of the tensile specimens.

Among the TR-UHPC tensile specimens, the CFT had the greatest improvement on the axial tensile properties of UHPC due to the excellent mechanical properties of the carbon fiber, which significantly increased the initial cracking strength and tensile strength by about 18.0% and 21.7%, respectively, compared to the plain UHPC specimens. The BFT-UHPC tensile specimens showed a second-grade increase in the initial cracking strength and tensile strength by about 12.0% and 15.9%, respectively. The surface impregnation treatment enhanced the firmness of the braided junction in the BFT compared to the other fiber textiles. At the microscopic level, the difference in thickness between the braided junction and other positions was more significant, resulting in the best bond with the matrix. Compared with the plain UHPC tensile specimen, the initial cracking strength and tensile

strength of the T-G2 specimens were improved by 9.1% and 8.0%, respectively. Though the improvement in the tensile performance of the T-G2 specimens was not obvious, there was a great improvement in ductility. It is possible that the surface treatment of CFT and GFT could enhance their interface bonding properties, resulting in more stable outcomes.

2.3.3. Impact of Textile Reinforcement Ratio on Tensile Properties of TR-UHPC Composites

For the sake of discussion, the critical textile reinforcement ratio of BFT should first be confirmed. It was assumed that there was no relative sliding between the fiber textile and the matrix before cracking of the UHPC matrix, namely, the fiber textile and UHPC matrix coordinated well in deformation. If the tensile strength of the TR-UHPC composite is expected to increase, the ultimate load of the inside fiber textile should be greater than the cracking load of the TR-UHPC composite. Considering the critical state, the formula for calculating the critical textile reinforcement ratio can be obtained:

$$\sigma_{cra} = E_f \varepsilon_{ct} V_f + E_c \varepsilon_{ct} (1 - V_f) \tag{1}$$

$$\sigma_{fu} V_{fmin} = \sigma_f V_{fmin} + \sigma_{ct} (1 - V_{fmin}) \tag{2}$$

$$V_{fmin} = \frac{\sigma_{ct}}{\sigma_{fu} + \sigma_{ct} - \sigma_f} \tag{3}$$

where σ_{cra} denotes the initial cracking stress of the TR-UHPC composite; E_f and E_c represent the modulus of elasticity of the fiber textile and UHPC matrix, respectively; ε_{ct} represents the matrix cracking strain; V_f represents the textile reinforcement ratio; σ_{fu} represents the ultimate strength of the fiber textile; V_{fmin} represents the critical minimum textile reinforcement ratio; σ_f denotes the stresses applied to the textile of the composite in the critical cracking state, and based on the assumption that the textile and matrix deform together before cracking, $\sigma_f = E_f \varepsilon_{ct}$; σ_{ct} represents the matrix cracking stress.

Figure 6 depicts the stress–strain curves of the tensile specimens with various BFT textile reinforcement ratios.

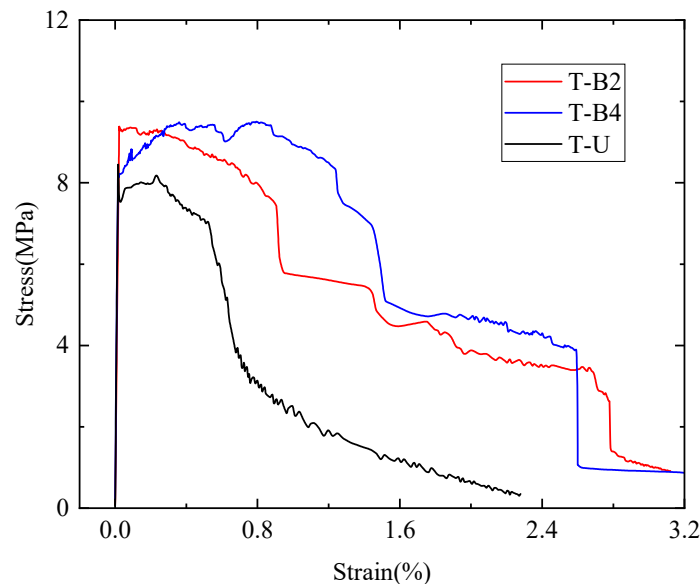


Figure 6. Comparison of the test results of different textile reinforcement ratios.

The critical textile reinforcement ratio of BFT is 0.36%. The T-B2 textile reinforcement ratio in this paper was 0.25%, which is close to the calculated critical textile reinforcement ratio and did not clearly show strain hardening characteristics after cracking. Compared with the T-U specimens, the T-B2 specimens had increases in their initial cracking strength and tensile strength of 12.0% and 16.0%, respectively. Furthermore, the descending stage of

the stress–strain curve of T-B2 was stable at a higher stress level, even though there was only one principal crack. The textile reinforcement ratio of T-B4 was 0.50%, which is greater than the critical textile reinforcement ratio. After cracking, T-B4 showed an obvious strain hardening stage. Additionally, the T-B4 specimens had a multi-cracking pattern compared to T-B2. The ultimate strain of T-B4 was 1.42%, which is about 1.4 times that of the T-B2 specimens, and 2.6 times that of the T-U specimens. The plummet in stress in the T-B series curves resulted from the rupture of the fiber bundles. After the fiber rupture, the T-B series specimens could also resist a high level of stress until failure.

3. Stacking and Bending Tests on BFT-UHPC Pedestrian Walkway Thin Slabs

3.1. Design and Manufacture of Test Slab

The BFT could perform as well as the CFT while costing only a twentieth of the price, making it a more economical option. Therefore, in this study, the BFT was selected to create the TR-UHPC composite slab specimen (BFT-UHPC slab) based on the results of the mechanical property tests and economic considerations. Figure 7 displays the dimensions and reinforcement layout of the test slab.

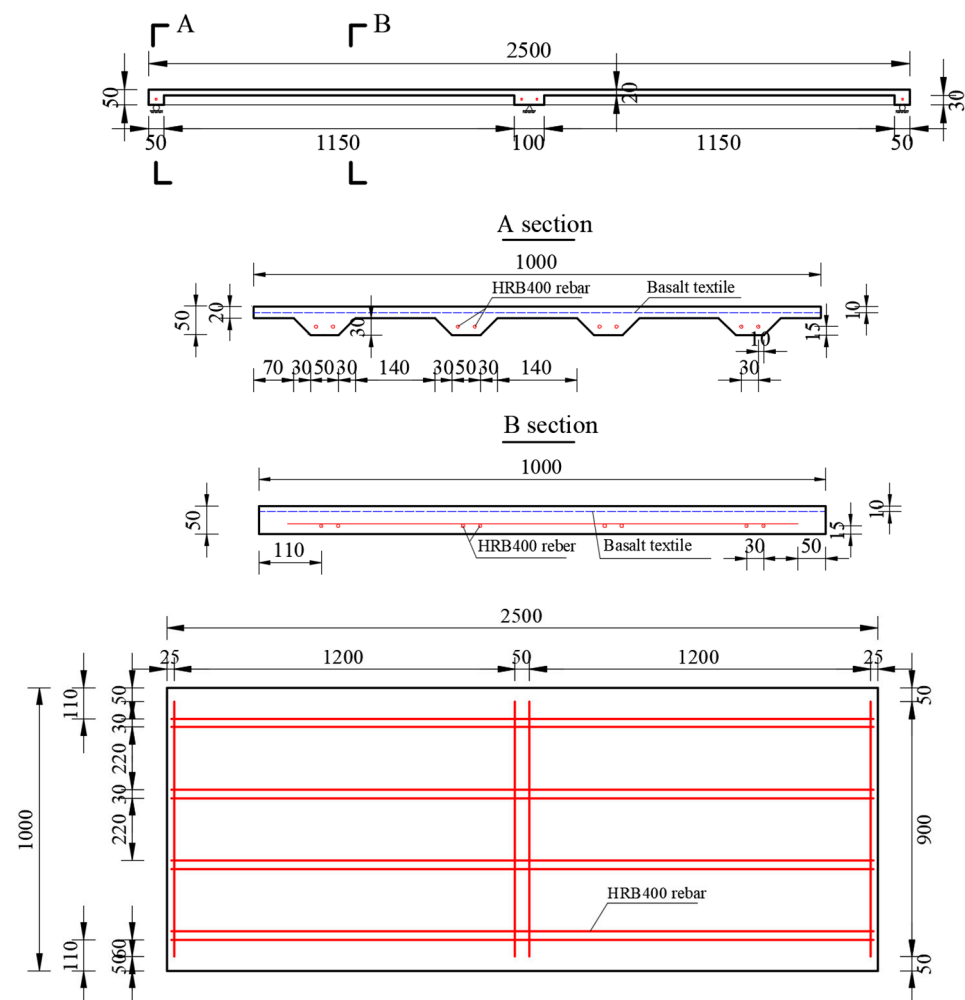


Figure 7. Dimension and reinforcement layout of the BFT-UHPC slab (mm).

A full-scale two-span continuous BFT-UHPC slab specimen was produced, measuring 2500 × 1000 × 50 mm overall. Each single span was 1175 mm long, with the upper flange part having a thickness of 20 mm. One layer of BFT was spread over the entire flange part with a 10 mm concrete cover. There were four longitudinal trapezoidal ribs with a rib height of 50 mm and a rib spacing of 250 mm, each reinforced with two Φ8 mm HRB400 rebars.

Three transverse rectangular ribs were made to support the slab. The transverse ribs at the end sections measured 50×30 mm and were reinforced by one $\Phi 8$ mm HRB400 rebar. The transverse rib at the mid-support section measured 100×30 mm and was reinforced by 2 $\Phi 8$ mm HRB400 rebars.

The manufacturing process of the BFT-UHPC slab specimen is as follows. (1) Fix the reinforcement cage, then cast the UHPC into the designated position for the BFTs. (2) Place the prepared BFT onto the fresh UHPC and gently press to ensure the UHPC surrounds the BFT. (3) Complete the casting of all the UHPC, then after 48 h of curing at room temperature, demold it and place it in steam at 90°C for 48 h. The casting process of the BFT-UHPC slab specimen is shown in Figure 8.



Figure 8. Specimen manufacturing process.

3.2. Material

The UHPC used in the stacking test was the same as that used in the axial tension tests but with some difference in their steel fiber components, that is, mixed steel fibers were used here, and the volume fraction of steel fibers was 3% [32,33], which consisted of 2% end-hooked steel fibers with a diameter of 0.2 mm and a length of 13 mm, and 1% short straight steel fibers with a diameter of 0.12 mm and a length of 8 mm.

In this section, the mechanical properties of the UHPC were assessed using the same test methods as in the previous section, as detailed in Table 6. The HRB400 rebar utilized for the mechanical properties test was sourced from the same batch as the test specimen. Its axial tensile mechanical properties were tested following the specifications outlined in GB/T228.1-2010 [34]. The material properties of the rebar are presented in Table 7.

Table 6. Mechanical properties of the UHPC of the BFT-UHPC slab.

Materials	f_{cu}/MPa	f_c/MPa	f_t/MPa	E_c/GPa
UHPC (Steam curing)	157.52	143.92	9.53	40.23

Table 7. Material performance data of the rebar.

Reinforcement Type	Diameter (mm)	Yield Strength (MPa)	Ultimate Strength (MPa)	Elasticity Modulus (GPa)
HRB400	8	429.3	590.3	200

3.3. Stacking Test

3.3.1. Experiment Program

The stacking test aimed to assess the workability of the BFT-UHPC slab under normal pedestrian usage conditions. The ‘General Specification for Highway Bridge and Culvert Design’ (JTG D60-2015) [35] recommends a uniform load of 4.0 kN/m^2 for the calculation of crowd load for pedestrian walkway slabs. To reproduce real-world conditions, the test slabs were loaded using a graded stacking of weights, categorized into two types: 10 kg and 5 kg. The constraint was provided by steel supports. Strain measurement points were positioned on the top and bottom surfaces of the positively and negatively bending sections. Throughout the loading process, vertical dial gauges were employed to measure

the deflections at two mid-spans and three supports. The loading setup and arrangement of measuring points are shown in Figure 9. The A-F in the figure refers to different areas of the test plate, A and B are the top of two mid-spans, C and D are the bottoms of two mid-spans (according to A and B), and J, Y and Z are the left, middle and right positions of the rebar respectively.

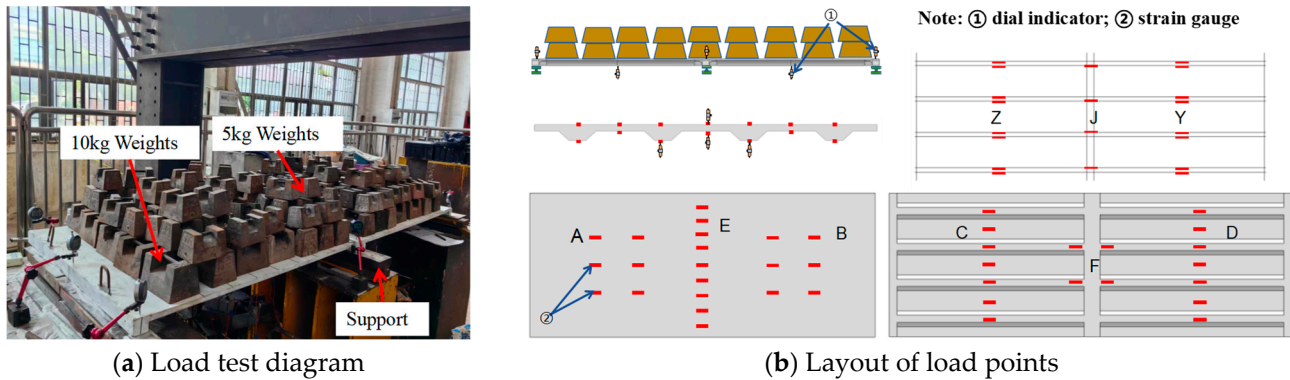


Figure 9. Loading setup and arrangement of the measuring points.

Following the stipulations in the ‘General Specification for Highway Bridge Design’ (JTG D60-2015) [35], the load was systematically applied in multiple levels, with each level consisting of a 250 kg load held for 10 min. A total of five loading levels were adopted.

3.3.2. Test Results

The test loading results are presented in Table 8. The single span of the test slab was 1175 mm, and the deflection limit for bridge deck members under the normal use limit state was 1/300 [35], equivalent to 3.92 mm. According to the specification [34], the mid-span deflection of the test slab under the standard 4 kN/m² load is 0.775 mm, which is merely 19.8% of the deflection limit, satisfying the requirements for the walking comfort of pedestrians. Additionally, based on the strain gauge data and visual observations, there was no occurrence of cracking damage on the BFT-UHPC slab, and the stiffness remained relatively unchanged, indicating that it still worked within the elastic stage. The mid-span bending moment *M* of continuous plate under uniform load was calculated as Equation (4).

$$M = \frac{ql^2}{64} \tag{4}$$

where *q* is the uniform load and *l* is the span.

Table 8. Results of the stacking test.

Loading Level	Loaded Weight (kg)	Uniform Load (kN/m ²)	Mean Deflection at Mid-Span (mm)	The Mid-Span Bending Moment <i>M</i> (kN·m)
0	0	0	0	0
1	250	1	0.156	0.219
2	500	2	0.321	0.441
3	750	3	0.459	0.658
4	1000	4	0.612	0.876
5	1250	5	0.775	1.096

3.4. Bending Test

3.4.1. Experiment Program

The bending test aimed to assess the ultimate bearing capacity of the BFT-UHPC slab under a five-point bending load. The test slab underwent point loading at the two mid-spans, and the measurement point arrangement was consistent with that of the stacking test.

The pre-cracking strain of UHPC was recorded using the corresponding surface-applied strain gauges. The loading setup and measurement point arrangement are illustrated in Figure 10.

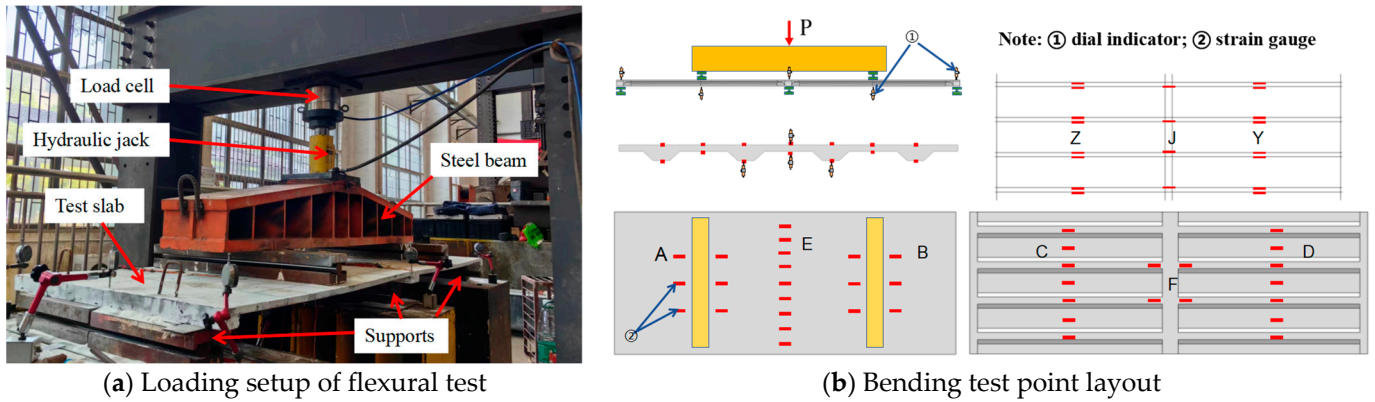


Figure 10. Flexural loading of the specimens and arrangement of the measuring points.

The test slab was loaded at a rate of 0.1 kN/s before cracking, with a load increase of 2 ± 0.3 kN per step. After cracking, the loading rate was maintained at 0.1 kN/s with a load increase of 5 ± 0.5 kN per step. The test slab was force-control loaded until reaching its ultimate bearing capacity. Subsequently, the deflection values in the two mid-spans of the test slab were used for displacement-control loading with a 0.15 mm increase per step. Once the load value dropped below 75% of the peak load, the test was considered complete and terminated.

3.4.2. Failure Mode and Stiffness Analysis

Figure 11 depicts the load–displacement curve of the BFT-UHPC slab, from which the damage process of the test slab can be divided into five stages.

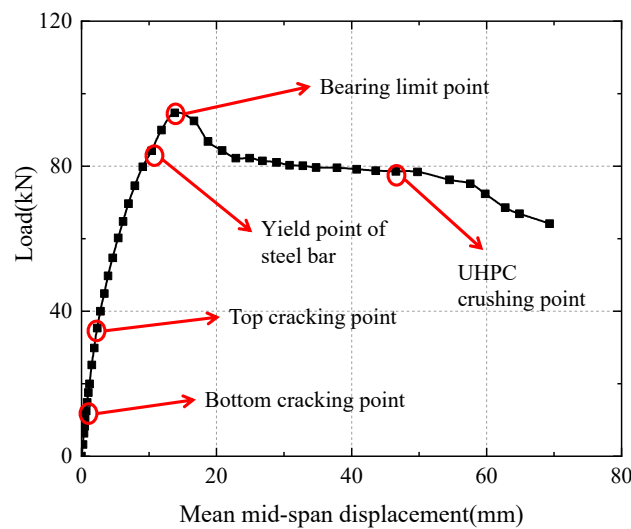


Figure 11. Load–displacement curve of the test slab.

Stage 1: Linear elasticity stage. Prior to UHPC cracking, the mid-span deflection varies linearly with increasing load.

Stage 2: Crack development stage (14.8 kN). Initially, numerous microcracks appeared at the bottom of the BFT-UHPC slab, causing no significant decrease in structural stiffness due to the strain-hardening properties of UHPC. The steel fibers in the matrix bridged the cracks and continued to provide tensile resistance. As loading continued, cracks developed

at the top of the slab near the support (Zone-E in Figure 10), resulting in a decrease in specimen stiffness. After the top UHPC cracked, the BFT started to perform, limiting the further development of UHPC cracks at the top while slowing the development of the bottom UHPC cracks.

Stage 3: Rebar yielding stage (84.2 kN). After the reinforcement yielded, UHPC entered the softening stage, gradually diminishing its contribution, which was accompanied by a decline in the specimen's stiffness. In this stage, the primary stressed section was the negatively bending section. The UHPC at the top of the slab entered the multi-cracking stage, and the textile and short steel fibers bore more external forces. With an increasing load, basalt fiber bundles and the matrix bridge anchorage between the fibers in the cracks played a dual role in transferring bridging forces, leading to the phenomenon of multi-crack development. When the UHPC crack spacing was insufficient, the basalt fiber bundles entered the tensile stage, gradually reaching the ultimate bearing capacity.

Stage 4: Peak load stage (94.7 kN). Due to the brittleness of the fibers, the test slab failed with the fiber rupture at the top of the support section. Prior to the rupture of fibers at the support section, the steel bars at the mid-span bottom yielded, causing a faster development in the crack width of the mid-span bottom than that of the support section. The negative bending zone could not bear more load after the fiber ruptured, leading to a decrease in the bearing capacity, and ultimately causing the test slab to fail. As the loading continued, the basalt fiber bundles sequentially reached their ultimate strength and ruptured, causing a reduction in the bearing capacity of the test slab. The UHPC crack at the top of the slab rapidly propagated to form a main crack, and the bearing section failed gradually. After the bottom of the slab took over as the main stress section, maintaining a certain level of bearing capacity, the UHPC crack development at the slab bottom accelerates. UHPC cracks gradually penetrated along the transverse direction at the mid-span (Zone-C), while on the other mid-span (Zone-D), UHPC cracks appeared to be partially closed.

Stage 5: Load declining stage. With consecutive loading, the top of the mid-span exhibited clear UHPC crushing, accompanied by the sound of steel fibers pulling out and UHPC matrix powder falling. The deflection at the crack location increased rapidly, leading to a significant decrease in the bearing capacity. The final failure mode of the BFT-UHPC slab is presented in Figure 12.

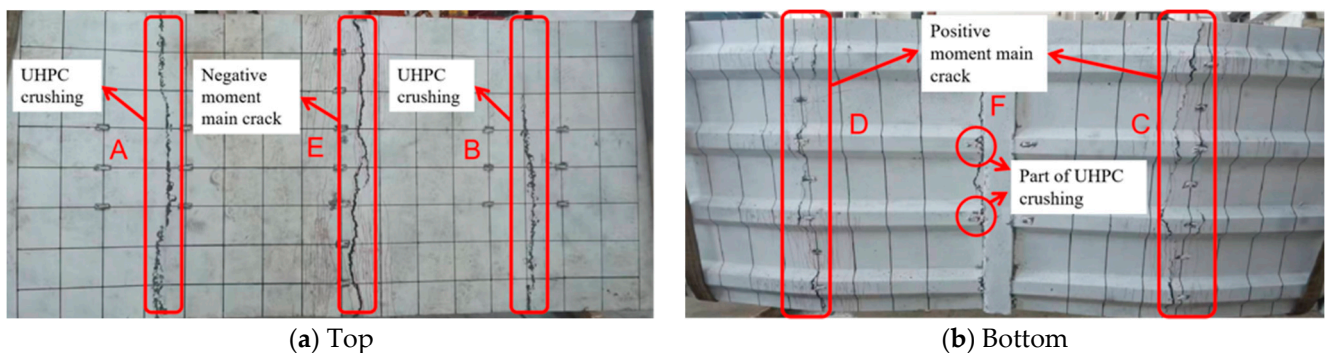


Figure 12. Specimen failure mode.

The test results indicate that upon reaching the failure state, the UHPC at the slab top was crushed, resulting in a substantial deflection without actual fracture. It was observed that the test slab not only exhibited a main crack in the negatively bending section, but also developed a main crack in the mid-span of the positively bending section on one side (Zone-C) during the load declining stage. The location of the lateral cracks generally corresponded to the main cracks on the slab soffits, and a multitude of small, dense UHPC cracks appeared in the soffit near the main crack. These cracks were mainly concentrated in the vicinity of the mid-span and mid-support sections.

Table 9 lists the characteristic loads of the BFT-UHPC slab. When the main crack width was equal to 0.2 mm (the limit for normal concrete), the rebars had already yielded, indicating that the BFT-UHPC is free of durability menace under normal usage. The $P_{bcr0.2}$ was about 5.7 times that of P_{cr} . If prestressing tendons can be used to replace the normal steel bar, the gap between the P_{cr} and $P_{bcr0.2}$ can be shortened significantly, which can be investigated in the future.

Table 9. Characteristic loads.

Eigenvalue	P_{cr} (kN)	$P_{bcr0.2}$ (kN)	$P_{tcr0.2}$ (kN)	P_y (kN)	P_u (kN)
Load	14.8	84.2	92.4	84.2	94.7

Note: In the table, P_{cr} is the cracking load of the test slab, $P_{bcr0.2}$ is the load when the crack width of the slab bottom is 0.2 mm, $P_{tcr0.2}$ is the load when the crack width of the slab top is 0.2 mm, P_y is the yield load of the test slab, and P_u is the ultimate bearing capacity of the slab.

3.4.3. Crack Width Development

The maximum crack width of a conventional rectangular RC slab with the same reinforcement ratio can be calculated using the crack width prediction formula for concrete bending structures specified in GB50010-2010 [36]. The crack width of the test slab is then compared to this value.

$$\omega_{max} = 1.9\psi \frac{\sigma_s}{E_s} \left(1.9c_s + 0.08 \frac{d_{eq}}{\rho_{te}} \right) \quad (5)$$

$$\psi = 1.1 - 0.65 \frac{f_{tk}}{\rho_{te}\sigma_s} \quad (6)$$

where ψ is the strain inhomogeneity coefficient of longitudinal tensile reinforcement between cracks; f_{tk} is the tensile strength of UHPC, which is 8.5 MPa; σ_s is the stress of steel bar in the support section under the corresponding load bending moment; E_s is the elastic modulus of reinforcement, which is 200 GPa; c_s is the thickness of the protective layer of the outermost steel bar, which is 35 mm; d_{eq} is the equivalent diameter of longitudinal reinforcement in the tension zone, which is 8 mm; ρ_{te} is the longitudinal tensile steel reinforcement ratio calculated from the section area of effective tensioned concrete, which is 1.4%.

Table 10 shows the calculation results for crack width. It is evident that the maximum crack width of the BFT-UHPC slab was lower than that of the RC slab at each loading stage. At the yield load (84.2 kN), the maximum crack width of the BFT-UHPC slab was only 35% of that of the conventional rectangular RC slab. This indicates that the BFT-UHPC slab has a superior crack resistance.

Table 10. Crack width correlation.

Load	39.9 kN	44.8 kN	54.7 kN	74.6 kN	84.2 kN
Specimen crack width (mm)	0.03	0.04	0.05	0.08	0.08
Crack width of concrete slab (mm)	0.05	0.06	0.11	0.15	0.23

4. Conclusions

In this study, basalt fiber textile (BFT) was identified as the most economical and effective reinforcement material for UHPC via axial tension experiments on textile-reinforced UHPC (TR-UHPC). Through stacking and bending tests, the workability and superior flexural behavior of the BFT-UHPC thin slab were examined. Based on the experimental study, some principal conclusions can be drawn.

- (1) In terms of the axial tensile performance, the fiber textiles ranked in the following order: CFT, BFT, and GFT. Furthermore, the corresponding increases in initial cracking strength and ultimate tensile strength were 18.0% and 21.9% for CFT, 12.0% and 16.0% for BFT, and only 9.1% and 8.0% for GFT, respectively.

- (2) When the textile reinforcement ratio was higher than the critical one, the specimen exhibited a clear strain hardening phenomenon after cracking. The T-B4 specimen showed a 12.0% increase in initial cracking strength and a 15.9% increase in tensile strength compared to the T-B2 specimen. The ultimate strain of T-B4 was 1.4 times that of T-B2 and 2.6 times that of the plain UHPC tensile specimen.
- (3) In the stacking test, the mid-span deflection of the BFT-UHPC slab was 0.775 mm under the crowd load (4 kN/m²), which was only 19.8% of the deflection limit, satisfying the walking comfort requirements of pedestrians. Therefore, the BFT-UHPC slab can remain uncracked during service.
- (4) The crack resistance and superior toughness of the BFT-UHPC composite have been well-verified. Fiber textiles play an important role in limiting the development of crack width, maintaining stiffness, and improving the ductility of the slab.

Author Contributions: Supervision, Y.Z.; Methodology, Y.Z.; Validation, Y.Q.; Formal analysis, Y.Q.; Investigation, J.F.; Data curation, J.F.; Writing—original draft, J.F.; Writing—review and editing, Y.Q. and Y.Z.; Supervision, Y.Z. All authors have read and agreed to the published version of the manuscript.

Funding: This study was financially supported by the Construction Science and Technology Project of Chongqing (ckz2022-1-9).

Institutional Review Board Statement: Not applicable.

Informed Consent Statement: Not applicable.

Data Availability Statement: The data presented in this study are available on request from the corresponding author. The data are not publicly available as the authors' future research work is strongly based on these.

Acknowledgments: We express our gratitude to Hunan Zhonglu Huacheng Bridge Technology Corporation (Xiangtan, China) for their help in preparing the specimens.

Conflicts of Interest: The authors declare no conflicts of interest.

References

1. Ministry of Transport. Ministry of Transport of the People's Republic of China. Statistical Bulletin on the Development of Transport Industry in 2022. China Transportation Report, 2023-06-16 (002). 2022. Available online: https://xxgk.mot.gov.cn/2020/jigou/zhghs/202306/t20230615_3847023.html (accessed on 16 June 2023). (In Chinese)
2. Shamsad, A. Reinforcement corrosion in concrete structures, its monitoring and service life prediction—A review. *Cem. Concr. Compos.* **2003**, *25*, 459–471.
3. Andrade, C. Propagation of reinforcement corrosion: Principles, testing and modelling. *Mater. Struct.* **2019**, *52*, 1–26. [CrossRef]
4. Kang, S.T.; Lee, Y.; Park, Y.D.; Kim, J.K. Tensile fracture properties of an ultra-high performance fibre reinforced concrete (UHPRC) with steel fiber. *Compos. Struct.* **2010**, *92*, 61–71. [CrossRef]
5. Tayeh, B.A.; Aadi, A.S.; Hilal, N.N.; Bakar, B.H.A.; Al-Tayeb, M.M.; Mansour, W.N. Properties of ultra-high performance fibre reinforced concrete (UHPRC): A Review Paper. *AIP Conf. Proc.* **2019**, *2157*, 20040e1.
6. Yang, K.; Long, G.; Tang, Z.; Wu, H.; Ma, G.; Cheng, Z.; Xiang, Y.; Xie, Y. Enhancement in strength and toughness of ultra-high performance concrete (UHPC) from micron- and nano-scale. *J. Build. Eng.* **2023**, *69*, 106308. [CrossRef]
7. Li, J.; Wua, Z.; Shi, C.; Yuan, Q.; Zhang, Z. Durability of ultra-high performance concrete—A review. *Constr. Build Mater* **2020**, *255*, 119296. [CrossRef]
8. Guo, Y.; Wang, J. Flexural behavior of high-strength steel bar reinforced UHPC beams with considering restrained shrinkage. *Constr. Build. Mater.* **2023**, *409*, 133802. [CrossRef]
9. Lai, Y.; Li, Y.; Huang, M.; Zhao, L.; Chen, J.; Xie, Y.M. Conceptual design of long span steel-UHPC composite network arch bridge. *Eng. Struct.* **2023**, *277*, 115434. [CrossRef]
10. CCPA-UHPC. 2022 China Ultra High Performance Concrete (UHPC) Technology and Application Development Report (Part II). *Concr. World* **2022**, *170*, 18–23. (In Chinese)
11. Chen, B.; Wu, H.; An, M.I.; Lee, G.C. Application of ultra-high performance concrete in bridge engineering in China. In Proceedings of the International Interactive Symposium on Ultra-High Performance Concrete, Des Moines, IA, USA, 18–20 July 2016; Iowa State University Digital Press: Ames, IA, USA, 2016; Volume 1. [CrossRef]
12. Joaquín, A.; Carvajal-Muñoz, J.S.; Ramírez-Munévar, C. Application of ultra-high-performance concrete as bridge pavement overlays: Literature review and case studies. *Constr. Build. Mater.* **2024**, *410*, 134221.

13. Li, C.; Shi, Y.; Zhou, J.; Fang, C.; He, J.; He, L. Experimental investigation on UHPC shrinkage of full-scale steel-UHPC composite bridge deck. *Dev. Built Environ.* **2023**, *16*, 100281.
14. Duan, Y.; Zhang, H.; Zhang, G.; Chen, P.; Li, X. Study on the Influence of Coupling Dynamic Performance of Rail-Railway Steel Truss Bridge. *Railw. Stand. Des.* **2024**, 1–7. (In Chinese)
15. Qiu, M.; Shao, X.; Wille, K.; Yan, B.; Wu, J. Experimental investigation on flexural behavior of reinforced ultra high performance concrete low-profile T-beams. *Int. J. Concr. Struct. Mater.* **2020**, *14*, 1–20. [[CrossRef](#)]
16. *JTG D62-2018*; Code for Design of Reinforced Concrete and Prestressed Concrete Bridges and Culverts for Highway. China Communication Press: Beijing, China, 2018. (In Chinese)
17. Song, L. Research on Application of ultra-high performance concrete in Bridge structure. *Railw. Constr. Technol.* **2022**, 82–86. (In Chinese) [[CrossRef](#)]
18. Chen, L. *Design and Application of High Strength and High Toughness Cement-Based Composite Pavement cover for High-Speed Railway*; Southwest Jiaotong University: Chengdu, China, 2018. (In Chinese)
19. Ala, T.; Brisid Isufi Davood, M.; António, P. Flexural strengthening of flat slabs with FRP composites using EBR and EBROG methods. *Eng. Struct.* **2020**, *211*, 110483. [[CrossRef](#)]
20. Kar, S.; Biswal, K. Hear strengthening of reinforced concrete T-Beams by using fiber-reinforced polymer composites: A data analysis. *Arab. J. Sci. Eng.* **2020**, *45*, 4203–4234. [[CrossRef](#)]
21. Zhai, M. *Research on Mechanical Properties and Application of Textile-Reinforced UHPC Materials*; Southeast University: Dhaka, Bangladesh, 2022. (In Chinese)
22. Contamine, R.; Larbi, A.; Hamelin, P. Contribution to direct tensile testing of textile reinforced concrete (TRC) composites. *Mater. Sci. Eng. A* **2011**, *528*, 8589–8598. [[CrossRef](#)]
23. Gong, T.; Ahmed, A.H.; Curosu, I.; Mechtcherine, V. Tensile behavior of hybrid fiber reinforced composites made of strain-hardening cement-based composites (SHCC) and carbon textile. *Constr. Build. Mater.* **2020**, *262*, 120913. [[CrossRef](#)]
24. Dong, Z.; Dai, J.; Deng, M.; Wu, Z. Experimental study on the mechanical properties of textile reinforced mortar (TRM) composites with different yarn shapes subjected to uniaxial tension. *Arch. Civil. Mech. Eng.* **2022**, *22*, 185. [[CrossRef](#)]
25. Meng, W.; Khayat, K.H.; Bao, Y. Flexural behaviors of fiber-reinforced polymer fabric reinforced ultra-high-performance concrete panels. *Cem. Concr. Compos.* **2018**, *93*, 43–53. [[CrossRef](#)]
26. *GB/T 50081-2019*; Test Method Standard for Physical and Mechanical Properties of Concrete. China Architecture and Construction Press: Beijing, China, 2019; pp. 18–25. (In Chinese)
27. *GB/T 31387-2015*; Reactive Powder Concrete. Standards Press of China: Beijing, China, 2015; pp. 8–9. (In Chinese)
28. Zhou, Z.; Zhang, Y.; Wang, Y.; Han, F.; Tian, H.; Peng, Z. Experimental study on tensile mechanical properties of mesh-reinforced UHPC thin plates. *J. Southeast Univ. (Nat. Sci. Ed.)* **2019**, *49*, 611–617. (In Chinese)
29. Hegger, J.; Will, N.; Bruckermann, O.; Voss, S. Load-bearing behaviour and simulation of textile reinforced concrete. *Mater. Struct.* **2006**, *39*, 765–776. [[CrossRef](#)]
30. Banholzer, B.; Brockmann, T.; Brameshuber, W. Material and bonding characteristics for dimensioning and modelling of textile reinforced concrete (TRC) elements. *Mater. Struct.* **2006**, *39*, 749–763. [[CrossRef](#)]
31. Xu, S.; Yan, Y.J. Axial tensile properties of concrete reinforced by fiber braided mesh with low distribution rate. *Compos. Mater.* **2011**, *28*, 206–213. (In Chinese)
32. Tanarlan, H.; Alver, N.; Jahangiri, R.; Yalçinkaya, Ç.; Yazıcı, H. Flexural strengthening of RC beams using UHPFRC laminates: Bonding techniques and rebar addition. *Eng. Struct.* **2017**, *155*, 45–55. [[CrossRef](#)]
33. Tanarlan, H. Flexural strengthening of RC beams with pretextileated ultra high performance fiber reinforced concrete laminates. *Eng. Struct.* **2017**, *151*, 337–348. [[CrossRef](#)]
34. *GB/T 228.1-2010*; Standardization Administration of China. Tensile test of Metal Materials. Standards Press of China: Beijing, China, 2010. (In Chinese)
35. *JTG D60-2015*; Industry Standard of the People’s Republic of China. General Code for Design of Highway Bridges and Culverts. People’s Communications Press Co., Ltd.: Beijing, China, 2015. (In Chinese)
36. *GB50010-2010*; Ministry of Housing and Urban-Rural Development of the People’s Republic of China. Code for Design of Concrete Structures. China Building and Construction Press: Beijing, China, 2010. (In Chinese)

Disclaimer/Publisher’s Note: The statements, opinions and data contained in all publications are solely those of the individual author(s) and contributor(s) and not of MDPI and/or the editor(s). MDPI and/or the editor(s) disclaim responsibility for any injury to people or property resulting from any ideas, methods, instructions or products referred to in the content.